

First Dark Matter Search Results from the LUX-ZEPLIN (LZ) Experiment

J. Aalbers,^{1,2} D.S. Akerib,^{1,2} C.W. Akerlof,³ A.K. Al Musalhi,⁴ F. Alder,⁵ A. Alqahtani,⁶ S.K. Alsum,⁷
C.S. Amarasinghe,³ A. Ames,^{1,2} T.J. Anderson,^{1,2} N. Angelides,^{5,8} H.M. Araújo,⁸ J.E. Armstrong,⁹ M. Arthurs,³
S. Azadi,¹⁰ A.J. Bailey,⁸ A. Baker,⁸ J. Balajthy,¹¹ S. Balashov,¹² J. Bang,⁶ J.W. Bargemann,¹⁰ M.J. Barry,¹³
J. Barthel,¹⁴ D. Bauer,⁸ A. Baxter,¹⁵ K. Beattie,¹³ J. Belle,¹⁶ P. Beltrame,^{5,17} J. Bensinger,¹⁸ T. Benson,⁷
E.P. Bernard,^{13,19} A. Bhatti,⁹ A. Biekert,^{13,19} T.P. Biesiadzinski,^{1,2} H.J. Birch,^{3,15} B. Birrittella,⁷
G.M. Blockinger,²⁰ K.E. Boast,⁴ B. Boxer,^{11,15} R. Bramante,^{1,2} C.A.J. Brew,¹² P. Brás,²¹ J.H. Buckley,²²
V.V. Bugaev,²² S. Burdin,¹⁵ J.K. Busenitz,²³ M. Buuck,^{1,2} R. Cabrera,²¹ C. Carels,⁴ D.L. Carlsmith,⁷ B. Carlson,¹⁴
M.C. Carmona-Benitez,²⁴ M. Cascella,⁵ C. Chan,⁶ A. Chawla,²⁵ H. Chen,¹³ J.J. Cherwinka,⁷ N.I. Chott,²⁶
A. Cole,¹³ J. Coleman,¹³ M.V. Converse,²⁷ A. Cottle,^{4,16} G. Cox,^{14,24} W.W. Craddock,¹ O. Creaner,¹³ D. Curran,¹⁴
A. Currie,⁸ J.E. Cutter,¹¹ C.E. Dahl,^{16,28} A. David,⁵ J. Davis,¹⁴ T.J.R. Davison,¹⁷ J. Delgado,¹⁴ S. Dey,⁴
L. de Viveiros,²⁴ A. Dobi,¹³ J.E.Y. Dobson,⁵ E. Druskiewicz,²⁷ A. Dushkin,¹⁸ T.K. Edberg,⁹ W.R. Edwards,¹³
M.M. Elnimr,²³ W.T. Emmet,²⁹ S.R. Eriksen,³⁰ C.H. Faham,¹³ A. Fan,^{1,2,*} S. Fayer,⁸ N.M. Fearon,⁴ S. Fiorucci,¹³
H. Flaecher,³⁰ P. Ford,¹² V.B. Francis,¹² E.D. Fraser,¹⁵ T. Fruth,^{4,5} R.J. Gaitskell,⁶ N.J. Gantos,¹³ D. Garcia,⁶
A. Geffre,¹⁴ V.M. Gehman,¹³ J. Genovesi,²⁶ C. Ghag,⁵ R. Gibbons,^{13,19} E. Gibson,⁴ M.G.D. Gilchriese,¹³
S. Gokhale,³¹ B. Gommer,⁷ J. Green,⁴ A. Greenall,¹⁵ S. Greenwood,⁸ M.G.D. van der Grinten,¹² C.B. Gwilliam,¹⁵
C.R. Hall,⁹ S. Hans,³¹ K. Hanzel,¹³ A. Harrison,²⁶ E. Hartigan-O'Connor,⁶ S.J. Haselschwardt,¹³ S.A. Hertel,³²
G. Heuermann,³ C. Hjelmfelt,²⁶ M.D. Hoff,¹³ E. Holtom,¹² J.Y.-K. Hor,²³ M. Horn,¹⁴ D.Q. Huang,^{3,6} D. Hunt,⁴
C.M. Ignarra,^{1,2} R.G. Jacobsen,^{13,19} O. Jahangir,⁵ R.S. James,⁵ S.N. Jeffery,¹² W. Ji,^{1,2} J. Johnson,¹¹
A.C. Kaboth,^{12,25,†} A.C. Kamaha,^{20,33} K. Kamdin,^{13,19} V. Kasey,⁸ K. Kazkaz,³⁴ J. Keefner,¹⁴ D. Khaitan,²⁷
M. Khaleeq,⁸ A. Khazov,¹² I. Khurana,⁵ Y.D. Kim,³⁵ C.D. Kocher,⁶ D. Kodroff,²⁴ L. Korley,^{3,18} E.V. Korolkova,³⁶
J. Kras,⁷ H. Kraus,⁴ S. Kravitz,¹³ H.J. Krebs,¹ L. Kreczko,³⁰ B. Krikler,³⁰ V.A. Kudryavtsev,³⁶ S. Kyre,¹⁰
B. Landerud,⁷ E.A. Leason,¹⁷ C. Lee,^{1,2} J. Lee,³⁵ D.S. Leonard,³⁵ R. Leonard,²⁶ K.T. Lesko,¹³ C. Levy,²⁰ J. Li,³⁵
F.-T. Liao,⁴ J. Liao,⁶ J. Lin,^{4,13,19} A. Lindote,²¹ R. Linehan,^{1,2} W.H. Lippincott,^{10,16} R. Liu,⁶ X. Liu,¹⁷ Y. Liu,⁷
C. Loniewski,²⁷ M.I. Lopes,²¹ E. Lopez Asamar,²¹ B. López Paredes,⁸ W. Lorenzon,³ D. Lucero,¹⁴ S. Luitz,¹
J.M. Lyle,⁶ P.A. Majewski,¹² J. Makkinje,⁶ D.C. Malling,⁶ A. Manalaysay,^{11,13} L. Manenti,⁵ R.L. Mannino,⁷
N. Marangou,⁸ M.F. Marzioni,¹⁷ C. Maupin,¹⁴ M.E. McCarthy,²⁷ C.T. McConnell,¹³ D.N. McKinsey,^{13,19}
J. McLaughlin,²⁸ Y. Meng,²³ J. Migneault,⁶ E.H. Miller,^{1,2,26} E. Mizrahi,^{9,34} J.A. Mock,^{13,20} A. Monte,^{10,16}
M.E. Monzani,^{1,2,37} J.A. Morad,¹¹ J.D. Morales Mendoza,^{1,2} E. Morrison,²⁶ B.J. Mount,³⁸ M. Murdy,³²
A.St.J. Murphy,¹⁷ D. Naim,¹¹ A. Naylor,³⁶ C. Nedlik,³² C. Nehr Korn,¹⁰ H.N. Nelson,¹⁰ F. Neves,²¹ A. Nguyen,¹⁷
J.A. Nikoleyczik,⁷ A. Nilima,¹⁷ J. O'Dell,¹² F.G. O'Neill,¹ K. O'Sullivan,^{13,19} I. Olcina,^{13,19} M.A. Olevitch,²²
K.C. Oliver-Mallory,^{8,13,19} J. Orpwood,³⁶ D. Pagenkopf,¹⁰ S. Pal,²¹ K.J. Palladino,^{4,7} J. Palmer,²⁵ M. Pangilinan,⁶
N. Parveen,²⁰ S.J. Patton,¹³ E.K. Pease,¹³ B. Penning,^{3,18} C. Pereira,²¹ G. Pereira,²¹ E. Perry,⁵ T. Pershing,³⁴
I.B. Peterson,¹³ A. Piepke,²³ J. Podczerwinski,⁷ D. Porzio,^{21,‡} S. Powell,¹⁵ R.M. Preece,¹² K. Pushkin,³
Y. Qie,²⁷ B.N. Ratcliff,¹ J. Reichenbacher,²⁶ L. Reichhart,⁵ C.A. Rhyne,⁶ A. Richards,⁸ Q. Riffard,^{13,19}
G.R.C. Rischbieter,²⁰ J.P. Rodrigues,²¹ A. Rodriguez,³⁸ H.J. Rose,¹⁵ R. Rosero,³¹ P. Rossiter,³⁶ T. Rushton,³⁶
G. Rutherford,⁶ D. Rynders,¹⁴ J.S. Saba,¹³ D. Santone,²⁵ A.B.M.R. Sazzad,²³ R.W. Schnee,²⁶ P.R. Scovell,^{4,12}
D. Seymour,⁶ S. Shaw,¹⁰ T. Shutt,^{1,2} J.J. Silk,⁹ C. Silva,²¹ G. Sinev,²⁶ K. Skarpaas,¹ W. Skulski,²⁷ R. Smith,^{13,19}
M. Solmaz,¹⁰ V.N. Solovov,²¹ P. Sorensen,¹³ J. Soria,^{13,19} I. Stancu,²³ M.R. Stark,²⁶ A. Stevens,^{4,5,8}
T.M. Stiegler,³⁹ K. Stifter,^{1,2,16} R. Studley,¹⁸ B. Suerfu,^{13,19} T.J. Sumner,⁸ P. Sutcliffe,¹⁵ N. Swanson,⁶
M. Szydagis,²⁰ M. Tan,⁴ D.J. Taylor,¹⁴ R. Taylor,⁸ W.C. Taylor,⁶ D.J. Temples,²⁸ B.P. Tennyson,²⁹ P.A. Terman,³⁹
K.J. Thomas,¹³ D.R. Tiedt,^{9,14,26} M. Timalina,²⁶ W.H. To,^{1,2} A. Tomás,⁸ Z. Tong,⁸ D.R. Tovey,³⁶ J. Tranter,³⁶
M. Trask,¹⁰ M. Tripathi,¹¹ D.R. Tronstad,²⁶ C.E. Tull,¹³ W. Turner,¹⁵ L. Tvrznikova,^{19,29,34} U. Utku,⁵
J. Va'vra,¹ A. Vacheret,⁸ A.C. Vaitkus,⁶ J.R. Verbus,⁶ E. Voirin,¹⁶ W.L. Waldron,¹³ A. Wang,^{1,2} B. Wang,²³
J.J. Wang,²³ W. Wang,^{7,32} Y. Wang,^{13,19} J.R. Watson,^{13,19} R.C. Webb,³⁹ A. White,⁶ D.T. White,¹⁰
J.T. White,^{39,‡} R.G. White,^{1,2} T.J. Whitis,^{1,10} M. Williams,^{3,18} W.J. Wisniewski,¹ M.S. Witherell,^{13,19}
F.L.H. Wolfs,²⁷ J.D. Wolfs,²⁷ S. Woodford,¹⁵ D. Woodward,^{24,§} S.D. Worm,¹² C.J. Wright,³⁰ Q. Xia,¹³
X. Xiang,⁶ Q. Xiao,⁷ J. Xu,³⁴ M. Yeh,³¹ J. Yin,²⁷ I. Young,¹⁶ P. Zarzhitsky,²³ A. Zuckerman,⁶ and E.A. Zweig³³

(The LUX-ZEPLIN (LZ) Collaboration)

¹SLAC National Accelerator Laboratory, Menlo Park, CA 94025-7015, USA

²Kavli Institute for Particle Astrophysics and Cosmology,

- 52 *Stanford University, Stanford, CA 94305-4085 USA*
 53 ³*University of Michigan, Randall Laboratory of Physics, Ann Arbor, MI 48109-1040, USA*
 54 ⁴*University of Oxford, Department of Physics, Oxford OX1 3RH, UK*
 55 ⁵*University College London (UCL), Department of Physics and Astronomy, London WC1E 6BT, UK*
 56 ⁶*Brown University, Department of Physics, Providence, RI 02912-9037, USA*
 57 ⁷*University of Wisconsin-Madison, Department of Physics, Madison, WI 53706-1390, USA*
 58 ⁸*Imperial College London, Physics Department, Blackett Laboratory, London SW7 2AZ, UK*
 59 ⁹*University of Maryland, Department of Physics, College Park, MD 20742-4111, USA*
 60 ¹⁰*University of California, Santa Barbara, Department of Physics, Santa Barbara, CA 93106-9530, USA*
 61 ¹¹*University of California, Davis, Department of Physics, Davis, CA 95616-5270, USA*
 62 ¹²*STFC Rutherford Appleton Laboratory (RAL), Didcot, OX11 0QX, UK*
 63 ¹³*Lawrence Berkeley National Laboratory (LBNL), Berkeley, CA 94720-8099, USA*
 64 ¹⁴*South Dakota Science and Technology Authority (SDSTA),*
 65 *Sanford Underground Research Facility, Lead, SD 57754-1700, USA*
 66 ¹⁵*University of Liverpool, Department of Physics, Liverpool L69 7ZE, UK*
 67 ¹⁶*Fermi National Accelerator Laboratory (FNAL), Batavia, IL 60510-5011, USA*
 68 ¹⁷*University of Edinburgh, SUPA, School of Physics and Astronomy, Edinburgh EH9 3FD, UK*
 69 ¹⁸*Brandeis University, Department of Physics, Waltham, MA 02453, USA*
 70 ¹⁹*University of California, Berkeley, Department of Physics, Berkeley, CA 94720-7300, USA*
 71 ²⁰*University at Albany (SUNY), Department of Physics, Albany, NY 12222-0100, USA*
 72 ²¹*Laboratório de Instrumentação e Física Experimental de Partículas (LIP),*
 73 *University of Coimbra, P-3004 516 Coimbra, Portugal*
 74 ²²*Washington University in St. Louis, Department of Physics, St. Louis, MO 63130-4862, USA*
 75 ²³*University of Alabama, Department of Physics & Astronomy, Tuscaloosa, AL 34587-0324, USA*
 76 ²⁴*Pennsylvania State University, Department of Physics, University Park, PA 16802-6300, USA*
 77 ²⁵*Royal Holloway, University of London, Department of Physics, Egham, TW20 0EX, UK*
 78 ²⁶*South Dakota School of Mines and Technology, Rapid City, SD 57701-3901, USA*
 79 ²⁷*University of Rochester, Department of Physics and Astronomy, Rochester, NY 14627-0171, USA*
 80 ²⁸*Northwestern University, Department of Physics & Astronomy, Evanston, IL 60208-3112, USA*
 81 ²⁹*Yale University, Department of Physics, New Haven, CT 06511-8499, USA*
 82 ³⁰*University of Bristol, H.H. Wills Physics Laboratory, Bristol, BS8 1TL, UK*
 83 ³¹*Brookhaven National Laboratory (BNL), Upton, NY 11973-5000, USA*
 84 ³²*University of Massachusetts, Department of Physics, Amherst, MA 01003-9337, USA*
 85 ³³*University of California, Los Angeles, Department of Physics & Astronomy, Los Angeles, CA 90095-1547*
 86 ³⁴*Lawrence Livermore National Laboratory (LLNL), Livermore, CA 94550-9698, USA*
 87 ³⁵*IBS Center for Underground Physics (CUP), Yuseong-gu, Daejeon, KOR*
 88 ³⁶*University of Sheffield, Department of Physics and Astronomy, Sheffield S3 7RH, UK*
 89 ³⁷*Vatican Observatory, Castel Gandolfo, V-00120, Vatican City State*
 90 ³⁸*Black Hills State University, School of Natural Sciences, Spearfish, SD 57799-0002, USA*
 91 ³⁹*Texas A&M University, Department of Physics and Astronomy, College Station, TX 77843-4242, USA*
 92 (Dated: July 7, 2022)

The LUX-ZEPLIN (LZ) experiment is a dark matter detector centered on a dual-phase xenon time projection chamber operating at the Sanford Underground Research Facility in Lead, South Dakota, USA. This Letter reports results from LZ's first search for Weakly Interacting Massive Particles (WIMPs) with an exposure of 60 live days using a fiducial mass of 5.5t. A profile-likelihood analysis shows the data to be consistent with a background-only hypothesis, setting new limits on spin-independent WIMP-nucleon cross-sections for WIMP masses above 9 GeV/c². The most stringent limit is set at 30 GeV/c², excluding cross sections above 5.9×10^{-48} cm² at the 90 % confidence level.

93 There is abundant astrophysical evidence for the ex- 104 ers [10–14], with telescopes [15–21], and in underground
 94 istence of dark matter [1–4], a nonrelativistic and non- 105 laboratories [22–29]. This Letter reports the first search
 95 baryonic matter component of the universe that has so 106 for dark matter from the LUX-ZEPLIN (LZ) experiment,
 96 far eluded direct detection through interaction with or- 107 with the largest target mass of any WIMP detection ex-
 97 dinary matter [5]. Weakly Interacting Massive Particles 108 periment to date.
 98 (WIMPs), which obtain their relic abundance by thermal 109 The LZ experiment [30, 31] is located 4850 ft un-
 99 freeze-out through weak interactions [6], are postulated 110 derground in the Davis Cavern at the Sanford Un-
 100 in a wide variety of viable extensions to the Standard 111 derground Research Facility (SURF) in Lead, South
 101 Model of particle physics [7–9]. They are a leading can- 112 Dakota, USA, shielded by an overburden of 4300 m
 102 didate to explain dark matter, despite strong constraints 113 water-equivalent [32]. It is a low-background, multi-
 103 from many searches completed and ongoing at collid- 114 detector experiment centered on a dual-phase time pro-

115 jection chamber (TPC) mounted in a double-walled ti- 171
 116 tanium cryostat [33] filled with 10t of liquid xenon 172
 117 (LXe). The TPC is a vertical cylinder approximately 173
 118 1.5 m in diameter and height, lined with reflective PTFE, 174
 119 and instrumented with 494 3-inch photomultiplier tubes 175
 120 (PMTs) in two arrays at top and bottom. Energy depo- 176
 121 sitions above approximately 1 keV in the 7 t active xenon 177
 122 region produce two observable signals: vacuum ultraviolet 178
 123 (VUV) scintillation photons (S1) and ionization elec- 179
 124 trons that drift under a uniform electric field to the liquid 180
 125 surface, where they are extracted and produce secondary 181
 126 scintillation in the xenon gas (S2). The ratio of S2 to S1 182
 127 differentiates interactions with a xenon nucleus (produc- 183
 128 ing a nuclear recoil, or NR) from interactions with the 184
 129 atomic electron cloud (producing an electron recoil, or 185
 130 ER).

131 The TPC is surrounded by two detectors, which pro- 187
 132 vide veto signals to reject internal and external back- 188
 133 grounds. A LXe “skin” detector between the TPC field 189
 134 cage and the cryostat wall is instrumented with 93 1-inch 190
 135 and 38 2-inch PMTs. The outer detector (OD) is a 191
 136 near-hermetic system of acrylic tanks containing 17 t of 192
 137 gadolinium-loaded (0.1 % by mass) liquid scintillator [34] 193
 138 to detect neutrons. The entire LZ detector system is 194
 139 in a tank filled with 238t of ultra-pure water to shield 195
 140 from the ambient radioactive background, and 120 8-inch 196
 141 PMTs are submersed in the water to record OD and wa- 197
 142 ter Cherenkov signals.

143 The data reported here were collected from 23 Dec 199
 144 2021 to 11 May 2022 under stable detector conditions. 200
 145 The cathode and gate electrodes [35] established a drift 201
 146 field of 193 V/cm, determined by electrostatic simulation 202
 147 to vary by 4 % over the volume considered in this anal- 203
 148 ysis. The gate and anode electrodes established a gas 204
 149 extraction field of 7.3 kV/cm at radial position $r = 0$. 205
 150 Twelve TPC and two skin PMTs developed malfunction- 206
 151 ing connections or excessive noise during commissioning 207
 152 and were disabled prior to the run. The temperature and 208
 153 pressure of the LXe were stable to within 0.2%, at 174.1 K 209
 154 (at the TPC bottom) and 1.791 bar(a). The liquid level 210
 155 was stable to within 10 μm , measured by precision capac- 211
 156 itance sensors. The full xenon complement of 10 t was 212
 157 continuously purified at 3.3 t/day through a hot getter 213
 158 system, and the observed electron lifetime against attach- 214
 159 ment on electronegative impurities was between 5000 μs 215
 160 and 8000 μs , much longer than the 951 μs maximum drift 216
 161 time in the TPC.

162 The data acquisition (DAQ) system records events 217
 163 triggered by a digital filter sensitive to S2 signals in the 218
 164 TPC, reaching full efficiency for S2 pulses with 6 ex- 219
 165 tracted electrons at a typical rate of 5 Hz. A time window 220
 166 of 2 ms before and 2.5 ms after each trigger is recorded, 221
 167 constituting an event. Zero-suppressed waveforms from 222
 168 all PMT channels, including low- and high-gain ampli- 223
 169 fication paths for TPC and OD PMTs, are recorded for 224
 170 every trigger with single photoelectron efficiencies aver-

aging 94 %, 86 %, and >95 % for the TPC, skin, and OD 225
 PMTs, respectively.

173 Event properties are reconstructed through analysis of 226
 174 the PMT waveform shapes, timings, and distributions. 227
 175 Raw waveform amplitudes are normalized by the PMT 228
 176 and amplifier gains and summed separately within the 229
 177 TPC, skin, and OD. Integrated waveform area is reported 230
 178 in photons detected (phd) at each PMT, accounting for 231
 179 the double photoelectron effect in response to VUV pho- 232
 180 tons [36, 37]. Pulse boundaries are identified on the 233
 181 summed waveforms using filters tuned for prototypical 234
 182 pulse shapes in each detector. Pulses in the TPC are fur- 235
 183 ther classified as S1 or S2 based on their hit pattern and 236
 184 pulse shape. S1 pulses are required to have signals above 237
 185 the electronic noise threshold in at least 3 PMTs. The 238
 186 time ordering of the most prominent S1 and S2 pulses 239
 187 in each event is then used to identify single-scatter (one 240
 188 S1 preceding one S2) and multi-scatter (one S1 preced- 241
 189 ing multiple S2s) events. The transverse (x, y) location 242
 190 of events is determined by the PMT hit pattern of S2 243
 191 light from the extracted electrons, using the MERCURY 244
 192 algorithm [38]. The algorithm was tuned using uniformly 245
 193 distributed radioactive sources in the TPC and has a 1σ 246
 194 resolution of 4 mm for S2 signals of 3000 phd. The reso- 247
 195 lution worsens by approximately a factor of two near the 248
 196 TPC wall due to asymmetric light collection at the TPC 249
 197 edge. The location along the cylinder (z) axis is inferred 250
 198 from the drift time, and has a 1σ resolution of 0.7 mm 251
 199 for events near the cathode electrode.

200 LZ uses radioactive sources to correct for spatial vari- 252
 201 ation in response across the TPC and to calibrate the 253
 202 detector response to ER and NR events. ER calibration 254
 203 events are obtained using dispersed sources $^{83\text{m}}\text{Kr}$ and 255
 204 $^{131\text{m}}\text{Xe}$ before and during the WIMP search and triti- 256
 205 ated methane (CH_3T) post-search. The tritium source is 257
 206 important for understanding the response to low energy 258
 207 ER events, the most prominent background component 259
 208 in the run. Localized NR calibration events are created 260
 209 using a deuterium-deuterium (DD) generator that emits 261
 210 monoenergetic 2.45 MeV neutrons [39–41] along a con- 262
 211 duct through the water tank and AmLi sources [42] de- 263
 212 ployed between the walls of the cryostat vessels.

213 Using the dispersed sources, the S1 signal is normal- 264
 214 ized to the geometric center of the detector, using a cor- 265
 215 rection in x, y , and drift time; this normalized value is 266
 216 called S1c. The S2 signal is normalized to a signal at 267
 217 the radial center and top (shortest drift time) of the 268
 218 detector; this normalized value is called S2c. The size 269
 219 of the S1 corrections is on average 9 % and comes pri- 270
 220 marily from variations in light collection efficiency and 271
 221 PMT quantum efficiency. The size of the S2 corrections 272
 222 is on average 11 % in the (x, y) plane and comes pri- 273
 223 marily from non-operational PMTs and extraction-field 274
 224 non-uniformity caused by electrostatic deflection of the 275
 225 gate and anode electrodes. The S2 correction in z is 276
 226 due to electron attachment on impurities and averages

227 7%. Corrected parameters are uniform across the TPC
228 to within 3%.

229 To reproduce the TPC response to ER and NR
230 events, detector and xenon response parameters of the
231 NEST 2.3.7 [43] ER model are tuned to match the
232 median and widths of the tritium calibration data in
233 $\log_{10}S2c-S1c$ space, and to match the reconstructed
234 energies of the ^{83m}Kr (41.5 keV), ^{129m}Xe (236 keV), and
235 ^{131m}Xe (164 keV) peaks. The photon detection effi-
236 ciency g_1 is determined to be 0.114 ± 0.002 phd/photon
237 and the gain of the ionization channel g_2 to be
238 47.1 ± 1.1 phd/electron [44]. The tritium data are
239 best modeled with the NEST recombination skewness
240 model [45] disabled, and comparisons between the tuned
241 model and tritium data using several statistical tests
242 show consistency throughout the full tritium ER distribu-
243 tion [46–49]. The ER model includes effects from electron
244 capture decays [50]. The parameters of the ER model
245 were propagated to the NEST NR model and found to be
246 in good agreement with DD calibration data, matching
247 NR band means and widths to better than 1% and 4%
248 in $\log_{10}S2c$, respectively. Figure 1 shows the tritium and
249 DD neutron data compared to the calibrated model.

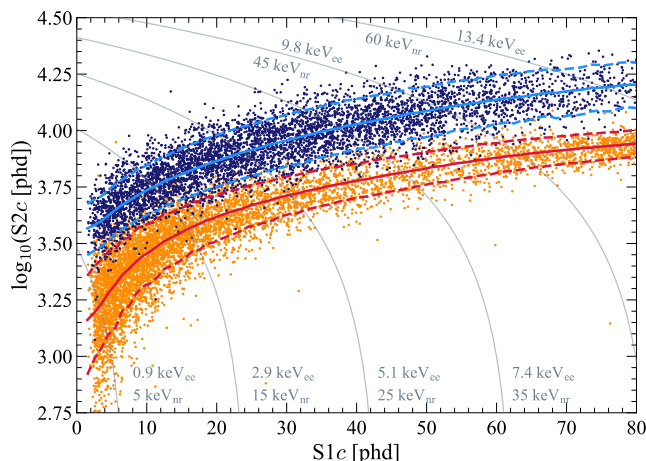


FIG. 1. Calibration events in $\log_{10}S2c-S1c$ for the tritium source (dark blue points, 5343 events) and the DD neutron source (orange points, 6324 events). Solid blue (red) lines indicate the median of the ER (NR) simulated distributions, and the dotted lines indicate the 10% and 90% quantiles. Thin grey lines show contours of constant electron-equivalent energy (keV_{ee}) and nuclear recoil energy (keV_{nr}).

250 The WIMP signal considered in this analysis is ex-
251 pected to produce low-energy, single-scatter NR signals
252 uniformly distributed in the TPC, with no additional sig-
253 nals in the TPC, skin, or OD. The following strategy is
254 used to obtain a clean sample of such events: exclude
255 time periods of elevated TPC activity or electronics in-
256 terference; remove multi-scatter interactions in the TPC;
257 remove events outside an energy region-of-interest (ROI);
258 remove events due to accidental coincidence of S1 and S2

259 pulses; remove events with coincident signals in the TPC
260 and skin or OD; remove events near the TPC active vol-
261 ume boundaries. Methods of bias mitigation that involve
262 obscuring the data, such as blinding the signal region, or
263 adding fake events (“salting”), were avoided to allow con-
264 trol over larger sources of systematic errors that may be
265 presented by a new detector. To mitigate bias in this
266 result, all analysis cuts were developed and optimized on
267 sideband selections and calibration data.

268 The search data set totals 89 live days after removing
269 periods for detector maintenance and calibration activity,
270 as well as a 3% loss due to DAQ dead time and a 7% loss
271 to periods excised due to anomalous trigger rates. Be-
272 cause dual-phase xenon TPCs experience elevated rates
273 of activity after large S2 pulses [25, 28, 51, 52], a time
274 hold-off is imposed to remove data taken after large S2s
275 and after cosmic-ray muons traversing the TPC. These
276 omissions result in a final search live time of 60 ± 1 d
277 where a WIMP interaction could be reconstructed. In
278 future searches, the hold-off can be relaxed by optimiza-
279 tion with respect to analysis cuts and detector operating
280 conditions.

281 The ROI is defined as S1c in the range 3 – 80 phd,
282 uncorrected S2 greater than 600 phd (>10 extracted elec-
283 trons), and S2c less than 10^5 phd, ensuring that signal effi-
284 ciencies are well understood and background ER sources
285 are well calibrated by the tritium data. Events classifi-
286 ed as multiple scatters in the TPC are removed, as are
287 events with poor reconstruction due to noise, spurious
288 pulses, or other data anomalies.

289 A suite of analysis cuts targets accidental coincidence
290 events, henceforth called “accidentals”, where an isolated
291 S1 and an isolated S2 are accidentally paired to mimic a
292 physical single-scatter event. Isolated S1s can be gener-
293 ated from sources such as particle interactions in charge-
294 insensitive regions of the TPC, Cherenkov and fluores-
295 cent light in detector materials, or dark-noise pile-up.
296 Isolated S2s can be generated from sources such as ra-
297 dioactivity or electron emission from the cathode or gate
298 electrodes, particle interactions in the gas phase or in
299 the liquid above the gate electrode, or drifting electrons
300 trapped on impurities and released with $\mathcal{O}(100\text{ ms})$ time
301 delay [52]. Analysis cuts to remove accidentals target
302 individual sources of isolated S1s and S2s using the ex-
303 pected behavior of the S1 and S2 pulses with respect
304 to quantities such as drift time, top-bottom asymme-
305 try of light, pulse width, timing of PMT hits within the
306 pulse, and hit pattern of the photons in the PMT arrays.
307 The cuts remove $>99.5\%$ of accidentals, measured using
308 single-scatter-like events with unphysical ($>951\ \mu\text{s}$) drift
309 time (UDT) and events generated by random matching
310 of isolated S1 and S2 populations.

311 Data-driven signal efficiencies for the trigger, recon-
312 struction, and analysis cuts are shown in Fig. 2. The
313 DAQ trigger efficiency is determined from DD data by
314 comparing the external trigger of the generator against

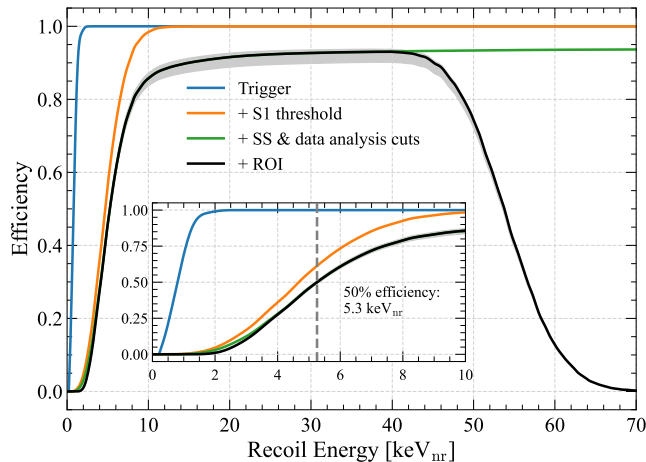


FIG. 2. Signal efficiency as a function of NR energy for the trigger (blue), the 3-fold coincidence and >3 phd threshold on S1 (orange), single-scatter (SS) reconstruction and analysis cuts (green), and the search ROI in S1 and S2 (black). The inset shows the low energy behavior, with the dotted line at $5.3 \text{ keV}_{\text{nr}}$ marking 50% efficiency. The error band (gray) is assessed using AmLi and tritium data as discussed in the text.

315 the TPC S2 trigger logic. The reconstruction efficiency
 316 for low-energy NR events is evaluated by comparing the
 317 reconstruction results against a large set of events manu-
 318 ally identified as single-scatter in DD data. Analysis cut
 319 efficiency is not determined directly from neutron cali-
 320 bration data as they do not cover the spatial extent of
 321 the TPC and are contaminated by a high rate of single
 322 photons and electrons. Instead, the efficiency through-
 323 out the full analysis volume is evaluated using tritium
 324 data for analysis cuts targeting S1 pulses and the combi-
 325 nation of tritium and AmLi data for those targeting S2
 326 pulses. Composite NR-like waveforms are generated using
 327 tritium single scatters with their S2 pulses replaced
 328 by smaller pulses from other tritium or AmLi events
 329 (an “AmLi-tritium” dataset). The uncertainty on the
 330 NR signal efficiency is the larger of the $\pm 1\sigma$ statistical
 331 fluctuation of the AmLi-tritium dataset and the differ-
 332 ence between the AmLi-tritium dataset and a pure AmLi
 333 dataset. The uncertainty is 3% for nuclear recoil energies
 334 $>3.5 \text{ keV}_{\text{nr}}$, increasing to 15% at $1 \text{ keV}_{\text{nr}}$.

335 Events with coincident activity in the TPC and skin or
 336 OD are removed to reduce backgrounds producing γ -rays
 337 and neutrons. To mitigate backgrounds associated with
 338 γ -rays, events with a prompt signal in the OD (skin)
 339 within $\pm 0.3 \mu\text{s}$ ($\pm 0.5 \mu\text{s}$) of the TPC S1 pulse are re-
 340 moved. Neutrons can thermalize in detector materials
 341 and those that capture on hydrogen or gadolinium in
 342 the OD can be tagged by an OD pulse of greater than
 343 $\sim 200 \text{ keV}$ within $1200 \mu\text{s}$ after the TPC S1. A selection
 344 on large skin pulses in the same time window addition-
 345 ally tags γ -rays returning to the xenon from an OD cap-
 346 ture process. AmLi calibration sources produce neutrons

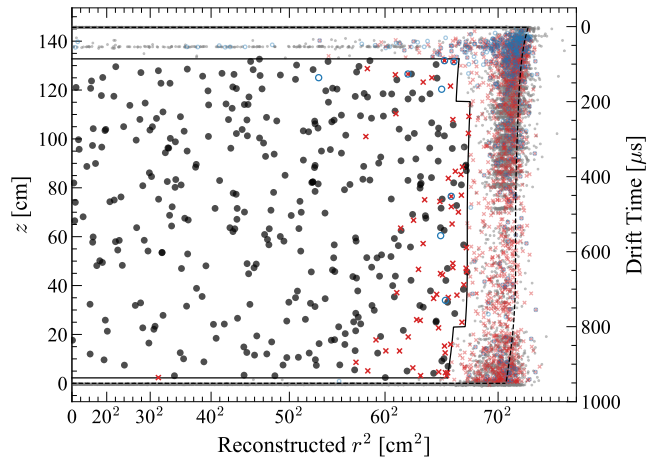


FIG. 3. Data in reconstructed r^2 and z after all analysis cuts. Black (grey) points show the data inside (outside) the FV. Red crosses and blue circles show events vetoed by a prompt LXe skin or OD signal, respectively. The solid line shows the FV definition, and the dashed line shows the extent of the active TPC. Field non-uniformities cause the reconstructed r position of the active volume boundary to vary as a function of z . Events with drift time of approximately $50 \mu\text{s}$ are from recoils in the gas which produce S1 and S2 pulses with a fixed time separation.

347 that scatter in both the TPC and the OD and are used
 348 to determine a neutron tagging efficiency for TPC single-
 349 scatters of $88.5 \pm 0.7\%$, with a false veto rate of 5% dom-
 350 inated by accidental activity in the OD during the coinci-
 351 dence window.

352 Finally, events outside a central fiducial volume (FV)
 353 are removed to reject external and other backgrounds
 354 which concentrate near the TPC boundaries, as shown
 355 in Fig. 3. Events at high radius have reduced position
 356 reconstruction resolution, due to reduced S2 light collec-
 357 tion efficiency and charge-loss effects within a few mil-
 358 limeters of the PTFE wall. The radial extent of the FV
 359 and the S2 threshold are chosen simultaneously to elim-
 360 inate events leaking into the FV due to poor position
 361 reconstruction resolution. Radially, the FV terminates
 362 at 4.0 cm in reconstructed position from the TPC wall,
 363 with small additional volumes removed in the top (5.2 cm
 364 for drift time $<200 \mu\text{s}$) and bottom (5.0 cm for drift time
 365 $>800 \mu\text{s}$) corners to account for increased rates of back-
 366 ground in those locations. Events within 6.0 cm of the
 367 (x, y) positions of two ladders of TPC field-cage resistors
 368 embedded in the TPC wall are also removed. Vertically,
 369 events with drift times $<86 \mu\text{s}$ and $>936.5 \mu\text{s}$ are rejected,
 370 corresponding to 12.8 cm and 2.2 cm from the gate and
 371 cathode electrodes, respectively. The xenon mass in the
 372 FV is estimated to be $5.5 \pm 0.2 \text{ t}$ using tritium data and
 373 confirmed by geometric calculation.

374 Figure 4 shows the distribution in $\log_{10} S2c-S1c$ of the
 375 335 events [53] passing all selections, along with con-

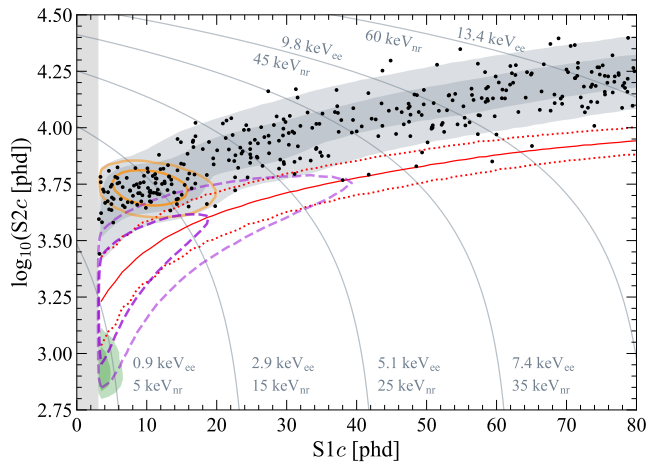


FIG. 4. WIMP-search data (black points) after all cuts in $\log_{10}S2c$ - $S1c$ space. Contours enclose 1σ and 2σ of the following models: the best-fit background model (shaded grey regions), the ^{37}Ar component (orange ellipses), a $30\text{ GeV}/c^2$ WIMP (purple dashed lines), and ^8B solar neutrinos (shaded green regions). The red solid line indicates the NR median, and the red dotted lines indicate the 10% and 90% quantiles. Model contours incorporate all efficiencies used in the analysis. Thin grey lines indicate contours of constant energy.

tours representing a $30\text{ GeV}/c^2$ WIMP, a flat NR distribution, and the background model. The signal model assumes spin-independent scattering from WIMPs with an isotropic Maxwell-Boltzmann velocity distribution, parameterized as in Ref. [54], with inputs from Refs. [55–60]. The WIMP model has an approximately exponentially decreasing energy spectrum with shape that depends on the mass of the WIMP [55].

The background model in this analysis consists of nine components, grouped according to their spectra in the ROI or the uncertainty on their rate. Table I lists the expected number of events from each component.

The dominant ER signal in the search comes from radioactive decay of impurities dispersed in the xenon. ^{214}Pb from the ^{222}Rn decay chain, ^{212}Pb from ^{220}Rn , and ^{85}Kr have broad energy spectra that are nearly flat in energy across the ROI and are summed into an overall β background. The concentrations of ^{214}Pb and ^{212}Pb are determined by fitting to energy peaks outside the ROI. The xenon was purified of krypton above ground using gas chromatography [61], and an *in situ* mass spectroscopy measurement of $144 \pm 22\text{ ppq } ^{\text{nat}}\text{Kr}$ (g/g) informs the ^{85}Kr rate estimate. The β component is further combined with a small ($<1\%$) and similarly flat ER contribution from γ -rays originating in the detector components [62] and cavern walls [63]. Solar neutrinos are also predicted to contribute a nearly flat ER spectrum in the ROI, with a rate calculated using Refs. [54, 64–66]. As the prediction is very precise, neutrinos are kept separate from the detector β background in this model.

TABLE I. Number of expected events from various sources for the $60\text{ d} \times 5.5\text{ t}$ exposure, before and after the combined fit of the background model plus a $30\text{ GeV}/c^2$ WIMP signal to the selected data. ^{37}Ar and detector neutrons have non-gaussian prior constraints and are totaled separately. Values at zero have no lower uncertainty due to the physical boundary.

Source	Expected Events	Best Fit
β decays + Det. ER	218 ± 36	222 ± 16
ν ER	27.3 ± 1.6	27.3 ± 1.6
^{127}Xe	9.2 ± 0.8	9.3 ± 0.8
^{124}Xe	5.0 ± 1.4	5.2 ± 1.4
^{136}Xe	15.2 ± 2.4	15.3 ± 2.4
^8B CE ν NS	0.15 ± 0.01	0.15 ± 0.01
Accidentals	1.2 ± 0.3	1.2 ± 0.3
Subtotal	276 ± 36	281 ± 16
^{37}Ar	$[0, 291]$	$52.1_{-8.9}^{+9.6}$
Detector neutrons	$0.0^{+0.2}$	$0.0^{+0.2}$
$30\text{ GeV}/c^2$ WIMP	–	$0.0^{+0.6}$
Total	–	333 ± 17

The naturally occurring isotopes of ^{124}Xe (double electron capture) and ^{136}Xe (double β decay) contribute ER events, and the predictions are driven by the known isotopic abundances, lifetimes, and decay schemes [67–69].

Cosmogenic activation of the xenon prior to underground deployment produces short-lived isotopes that decayed during this first run, notably ^{127}Xe (36.3 d) and ^{37}Ar (35.0 d) [70–72]. Atomic de-excitations following ^{127}Xe L- or M-shell electron captures fall within the ROI if the ensuing ^{127}I nuclear de-excitation γ -ray(s) escapes the TPC. The rate of ^{127}Xe electron captures is constrained by the rate of K-shell atomic de-excitations, which are outside the ROI. The skin is effective at tagging the ^{127}I nuclear de-excitation γ -ray(s), reducing this background by a factor of 5. The number of ^{37}Ar events is estimated by calculating the exposure of the xenon to cosmic rays before it was brought underground, then correcting for the decay time before the search [73]. A flat constraint of 0 to three times the estimate of 97 events is imposed because of large uncertainties on the prediction.

The NR background has contributions from radiogenic neutrons and coherent elastic neutrino-nucleus scattering (CE ν NS) from ^8B solar neutrinos. The prediction for the CE ν NS rate, calculated as in Refs. [54, 64–66], is small due to the $S2 > 600$ phd requirement. The rate of radiogenic neutrons in the ROI is constrained using the distribution of single scatters in the FV tagged by the OD and then applying the measured neutron tagging efficiency ($88.5 \pm 0.7\%$). A likelihood fit of the NR component in the OD-tagged data is consistent with observing zero events, leading to a data-driven constraint of $0.0^{+0.2}$ applied to the search. This rate agrees with simulations based on detector material radioassay [62].

Finally, the expected distribution of accidentals is de-

440 terminated by generating composite single-scatter event
 441 waveforms from isolated S1 and S2 pulses and applying
 442 the WIMP analysis selections. The selection efficiency
 443 is then applied to UDT single-scatter-like events to con-
 444 strain the accidentals rate.

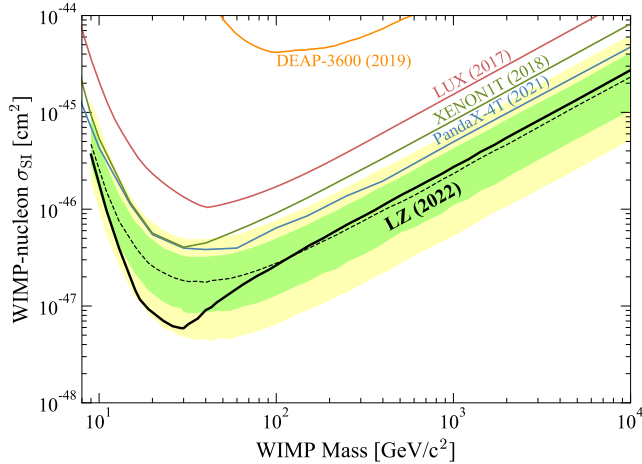


FIG. 5. The 90% confidence limit (black line) for the spin-independent WIMP cross section vs. WIMP mass. The green and yellow bands are the 1σ and 2σ sensitivity bands. The dotted line shows the median of the sensitivity projection. Also shown are the PandaX-4T [26], XENON1T [25], LUX [28], and DEAP-3600 [74] limits.

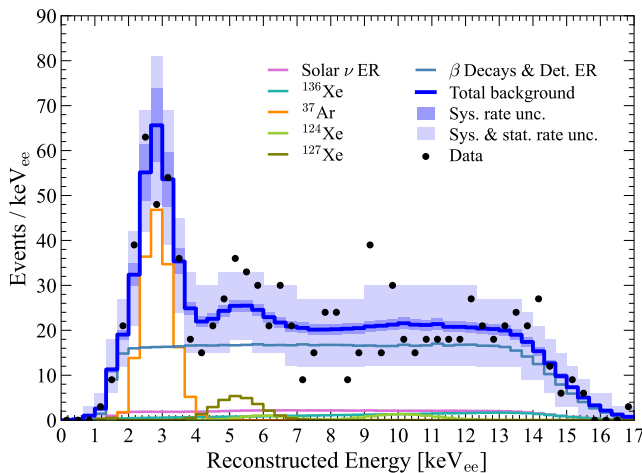


FIG. 6. Reconstructed energy spectrum of the best fit model. Data points are shown in black. The blue line shows total summed background. The darker blue band shows the model uncertainty and the lighter blue band the combined model and statistical uncertainty. Background components are shown in colors as given in the legend. Background components from ^8B solar neutrinos and accidentals are included in the fit but are too small to be visible in the plot.

445 Statistical inference of WIMP scattering cross section
 446 and mass is performed with an extended unbinned pro-
 447 file likelihood statistic in the $\log_{10}S2c\text{-}S1c$ observable

448 space, with a two-sided construction of the 90% confi-
 449 dence bounds [54]. Background and signal component
 450 shapes are modeled in the observable space using the
 451 GEANT4-based package BACCARAT [75, 76] and a custom
 452 simulation of the LZ detector response using the tuned
 453 NEST model. The background component uncertainties
 454 are included as constraint terms in a combined fit of the
 455 background model to the data, the result of which is also
 456 shown in Table I.

457 Above the smallest tested WIMP mass of $9\text{ GeV}/c^2$,
 458 the best-fit number of WIMP events is zero, and the data
 459 are thus consistent with the background-only hypothesis.
 460 Figure 5 shows the 90% confidence level upper limit on
 461 the spin-independent WIMP-nucleon cross section σ_{SI} as
 462 a function of mass. The minimum of the limit curve is at
 463 $m_\chi = 30\text{ GeV}/c^2$ with a limit of $\sigma_{\text{SI}} = 5.9 \times 10^{-48}\text{ cm}^2$.
 464 For WIMP masses between $19\text{ GeV}/c^2$ and $26\text{ GeV}/c^2$,
 465 background fluctuations produce a limit which is below
 466 a critical discovery power threshold, $\pi_{\text{crit}} = 0.32$, and
 467 for these masses the reported limit is set to the limit
 468 equivalent to π_{crit} [54]. The background model and data
 469 as a function of reconstructed energy are shown in Fig. 6,
 470 and the data agree with the background-only model with
 471 a p-value of 0.96. A data release for this result is in the
 472 Supplemental Materials [77].

473 The LZ experiment has achieved the highest sensitivity
 474 to spin-independent WIMP-nucleon scattering for masses
 475 greater than $9\text{ GeV}/c^2$ due to the successful operation
 476 of an integrated detector system containing the largest
 477 dual-phase xenon TPC to date. LZ is continuing opera-
 478 tions at SURF and will undertake further detector and
 479 analysis optimization to search for a broad range of rare-
 480 event physics searches, including WIMPs, neutrinoless
 481 double-beta decay, solar neutrinos, and solar axions [78–
 482 80] over an estimated 1000 day exposure.

483 The research supporting this work took place in part
 484 at SURF in Lead, South Dakota. Funding for this work
 485 is supported by the U.S. Department of Energy, Office of
 486 Science, Office of High Energy Physics under Contract
 487 Numbers DE-AC02-05CH11231, DE-SC0020216, DE-
 488 SC0012704, DE-SC0010010, DE-AC02-07CH11359,
 489 DE-SC0012161, DE-SC0015910, DE-SC0014223,
 490 DE-SC0010813, DE-SC0009999, DE-NA0003180,
 491 DE-SC0011702, DE-SC0010072, DE-SC0015708, DE-
 492 SC0006605, DE-SC0008475, DE-SC0019193, DE-
 493 FG02-10ER46709, UW PRJ82AJ, DE-SC0013542,
 494 DE-AC02-76SF00515, DE-SC0018982, DE-SC0019066,
 495 DE-SC0015535, DE-SC0019319, DE-AC52-07NA27344,
 496 & DOE-SC0012447. This research was also sup-
 497 ported by U.S. National Science Foundation (NSF);
 498 the UKRI's Science & Technology Facilities Council
 499 under award numbers ST/M003744/1, ST/M003655/1,
 500 ST/M003639/1, ST/M003604/1, ST/M003779/1,
 501 ST/M003469/1, ST/M003981/1, ST/N000250/1,
 502 ST/N000269/1, ST/N000242/1, ST/N000331/1,
 503 ST/N000447/1, ST/N000277/1, ST/N000285/1,

ST/S000801/1, ST/S000828/1, ST/S000739/1,
 ST/S000879/1, ST/S000933/1, ST/S000844/1,
 ST/S000747/1, ST/S000666/1, ST/R003181/1; Por-
 tuguese Foundation for Science and Technology (FCT)
 under award numbers PTDC/FIS-PAR/2831/2020; the
 Institute for Basic Science, Korea (budget number IBS-
 R016-D1). We acknowledge additional support from the
 STFC Boulby Underground Laboratory in the U.K., the
 GridPP [81, 82] and IRIS Collaborations, in particular
 at Imperial College London and additional support by
 the University College London (UCL) Cosmoparticle
 Initiative. We acknowledge additional support from the
 Center for the Fundamental Physics of the Universe,
 Brown University. K.T. Lesko acknowledges the support
 of Brasenose College and Oxford University. The LZ
 Collaboration acknowledges key contributions of Dr.
 Sidney Cahn, Yale University, in the production of
 calibration sources. This research used resources of the
 National Energy Research Scientific Computing Center,
 a DOE Office of Science User Facility supported by the
 Office of Science of the U.S. Department of Energy un-
 der Contract No. DE-AC02-05CH11231. We gratefully
 acknowledge support from GitLab through its GitLab
 for Education Program. The University of Edinburgh
 is a charitable body, registered in Scotland, with the
 registration number SC005336. The assistance of SURF
 and its personnel in providing physical access and
 general logistical and technical support is acknowledged.
 We acknowledge the South Dakota Governor's office,
 the South Dakota Community Foundation, the South
 Dakota State University Foundation, and the University
 of South Dakota Foundation for use of xenon. We also
 acknowledge the University of Alabama for providing
 xenon.

* afan@slac.stanford.edu

† asher.kaboth@rhul.ac.uk

‡ Deceased

§ dwoodward@psu.edu

- [1] Aghanim, N. *et al.* (Planck Collaboration), *Astron. Astrophys.* **641**, A6 (2020).
- [2] Y. Sofue and V. Rubin, *Annu. Rev. Astron. Astrophys.* **39**, 137 (2001).
- [3] D. Harvey, R. Massey, T. Kitching, A. Taylor, and E. Tittley, *Science* **347**, 1462 (2015).
- [4] A. Arbey and F. Mahmoudi, *Prog. Part. Nucl. Phys.* **119**, 103865 (2021).
- [5] M. Schumann, *J. Phys G* **46**, 103003 (2019).
- [6] B. W. Lee and S. Weinberg, *Phys. Rev. Lett.* **39**, 165 (1977).
- [7] G. Bertone and D. Hooper, *Rev. Mod. Phys.* **90**, 045002 (2018).
- [8] J. Billard *et al.*, *Rep. Progress. Phys.* **85**, 056201 (2022).
- [9] D. Akerib *et al.*, arXiv preprint arXiv:2203.08084 <https://doi.org/10.48550/arXiv.2203.08084> (2022).
- [10] M. Aaboud *et al.* (ATLAS Collaboration), *J. High En-*

ergy Phys. **2018** (1), 1.

- [11] A. M. Sirunyan *et al.* (CMS Collaboration), *Phys. Rev. D* **97**, 092005 (2018).
- [12] M. Aaboud *et al.* (ATLAS Collaboration), *Phys. Lett. B* **776**, 318 (2018).
- [13] A. M. Sirunyan *et al.* (CMS Collaboration), *Eur. Phys. J. C* **78**, 1 (2018).
- [14] N. Trevisani, *Universe* **4**, 10.3390/universe4110131 (2018).
- [15] K. Abe *et al.* (Super-Kamiokande Collaboration), *Phys. Rev. D* **102**, 072002 (2020).
- [16] K. Choi *et al.* (Super-Kamiokande Collaboration), *Phys. Rev. Lett.* **114**, 141301 (2015).
- [17] R. Abbasi *et al.* (IceCube Collaboration), *Phys. Rev. D* **105**, 062004 (2022).
- [18] A. Albert *et al.* (ANTARES Collaboration), *Phys. Lett. B* **769**, 249 (2017).
- [19] A. Cuoco, M. Krämer, and M. Korsmeier, *Phys. Rev. Lett.* **118**, 191102 (2017).
- [20] M.-Y. Cui, Q. Yuan, Y.-L. S. Tsai, Y.-Z. Fan, *et al.*, *Phys. Rev. Lett.* **118**, 191101 (2017).
- [21] A. Albert *et al.*, *Astrophys J* **834**, 110 (2017).
- [22] A. Abdelhameed *et al.* (CRESST Collaboration), *Phys. Rev. D* **100**, 102002 (2019).
- [23] P. Agnes *et al.* (DarkSide-50 Collaboration), *Phys. Rev. Lett.* **121**, 081307 (2018).
- [24] C. Amole *et al.* (PICO Collaboration), *Phys. Rev. D* **100**, 022001 (2019).
- [25] E. Aprile *et al.* (XENON Collaboration), *Phys. Rev. Lett.* **121**, 111302 (2018).
- [26] Y. Meng *et al.* (PandaX-4T Collaboration), *Phys. Rev. Lett.* **127**, 261802 (2021).
- [27] R. Ajaj *et al.* (DEAP Collaboration), *Phys. Rev. D* **100**, 022004 (2019).
- [28] D. Akerib *et al.* (LUX Collaboration), *Phys. Rev. Lett.* **118**, 021303 (2017).
- [29] R. Agnese *et al.* (SuperCDMS Collaboration), *Phys. Rev. D* **92**, 072003 (2015).
- [30] D. Akerib *et al.* (LZ Collaboration), *Nucl. Instrum. Methods Phys. Res. Sect. A* **953**, 163047 (2020).
- [31] B. Mount *et al.*, arXiv preprint arXiv:1703.09144 <https://doi.org/10.48550/arXiv.1703.09144> (2017).
- [32] J. Heise, *J. Phys. Conf. Ser.* **2156**, 012172 (2021).
- [33] D. Akerib *et al.* (LZ Collaboration), *Astropart. Phys.* **96**, 1 (2017).
- [34] S. J. Haselschwardt, S. Shaw, H. N. Nelson, M. S. Withereil, M. Yeh, K. T. Lesko, A. Cole, S. Kyre, and D. T. White, *Nucl. Instrum. Meth. A* **937**, 148 (2019), arXiv:1808.05595 [physics.ins-det].
- [35] R. Linehan *et al.*, *Nucl. Instrum. Methods Phys. Res., Sect. A* **1031**, 165955 (2022).
- [36] C. Faham, V. Gehman, A. Currie, A. Dobi, P. Sorensen, and R. Gaitskell, *JINST* **10** (09), P09010.
- [37] B. López Paredes, H. Araújo, F. Froberg, N. Marangou, I. Olcina, T. Sumner, R. Taylor, A. Tomás, and A. Vacheret, *Astropart. Phys.* **102**, 56 (2018).
- [38] V. N. Solovov *et al.*, *IEEE Trans. on Nucl. Sci.* **59**, 3286 (2012).
- [39] A. Chen, C. Gary, E. Guan, G. Jones, M. Piestrup, and G. Smith, Adelphi Technologies, Inc., 2003 East Bayshore Rd, Redwood City, CA 94063.
- [40] J. R. Verbus *et al.*, *Nucl. Instrum. Methods Phys. Res., Sect. A* **851**, 68–81 (2017).
- [41] D. S. Akerib *et al.*, arXiv:1608.05381 [astro-ph,

- physics:hep-ex, physics:physics] (2016), arXiv: 687 1608.05381.
- [42] A. V. Mozhayev, M. E. Moore, and E. K. Mace, Appl. 688 Radiat. Isot. **168**, 109472 (2021).
- [43] M. Szydagis *et al.*, Noble Element Simulation Technique 689 (2022).
- [44] See Supplemental Material at [please.insert.a.url](#) for 690 the full description of the NEST parameters and a header 691 file to configure the software for this model.
- [45] D. Akerib *et al.* (LUX Collaboration), Phys. Rev. D **102**, 692 112002 (2020).
- [46] A. Kolmogorov, Inst. Ital. Attuari, Giorn. **4**, 83 (1933).
- [47] N. V. Smirnov, Bull. Math. Univ. Moscou **2**, 3 (1939).
- [48] T. W. Anderson and D. A. Darling, Ann. Math. Stat. **23**, 693 193 (1952).
- [49] S. S. Shapiro and M. B. Wilk, Biometrika **52**, 591 (1965).
- [50] D. J. Temples *et al.*, Phys. Rev. D **104**, 112001 (2021).
- [51] P. Sorensen, arXiv preprint arXiv:1702.04805 694 <https://doi.org/10.48550/arXiv.1702.04805> (2017).
- [52] D. S. Akerib *et al.* (LUX Collaboration), Phys. Rev. D 695 **102**, 092004 (2020).
- [53] See Supplemental Material at [please.insert.a.url](#) for 696 a detailed table of events by selection.
- [54] D. Baxter *et al.*, Eur. Phys. J. C **81**, 1 (2021).
- [55] J. Lewin and P. Smith, Astropart. Phys. **6**, 87 (1996).
- [56] M. C. Smith *et al.*, Mon. Not. R. Astron. Soc. **379**, 755 697 (2007).
- [57] C. McCabe, J. Cosmol. Astropart. Phys. **2014** (02), 027.
- [58] R. Schönrich, J. Binney, and W. Dehnen, Mon. Not. R. 698 Astron. Soc. **403**, 1829 (2010).
- [59] J. Bland-Hawthorn and O. Gerhard, Annu. Rev. Astron. 699 Astrophys. **54**, 529 (2016).
- [60] Abuter, R. *et al.* (GRAVITY Collaboration), Astron. As- 700 trophys. **647**, A59 (2021).
- [61] D. Akerib *et al.*, Astropart. Phys. **97**, 80 (2018).
- [62] D. Akerib *et al.* (LZ Collaboration), Eur. Phys. J. C **80**, 1 (2020).
- [63] D. Akerib *et al.*, Astropart. Phys. **116**, 102391 (2020).
- [64] M. Agostini *et al.* (Borexino Collaboration), Phys. Rev. 699 D **100**, 082004 (2019).
- [65] N. Vinyoles *et al.*, Astrophys. J. **835**, 202 (2017).
- [66] B. Aharmim *et al.* (SNO Collaboration), Phys. Rev. C 699 **88**, 025501 (2013).
- [67] M. Berglund and M. E. Wieser, Pure Appl. Chem. **83**, 699 397 (2011).
- [68] E. Aprile *et al.* (XENON Collaboration), Nature **568**, 699 532 (2019).
- [69] J. B. Albert *et al.* (EXO Collaboration), Phys. Rev. C 699 **89**, 015502 (2014).
- [70] M.-M. Bé *et al.*, *Table of Radionuclides*, Monographie 699 BIPM-5, Vol. 7 (Bureau International des Poids et 699 Mesures, Pavillon de Breteuil, F-92310 Sèvres, France, 699 2013).
- [71] M.-M. Bé *et al.*, *Table of Radionuclides*, Monographie 699 BIPM-5, Vol. 8 (Bureau International des Poids et 699 Mesures, Pavillon de Breteuil, F-92310 Sèvres, France, 699 2016).
- [72] D. S. o. Akerib (LUX Collaboration), Phys. Rev. D **96**, 699 112011 (2017).
- [73] J. Aalbers *et al.* (LZ Collaboration), Phys. Rev. D **105**, 699 082004 (2022).
- [74] P.-A. Amaudruz *et al.* (DEAP Collaboration), Phys. Rev. 699 Lett. **121**, 071801 (2018).
- [75] D. Akerib *et al.* (LZ Collaboration), Astropart. Phys. 699 **125**, 102480 (2021).
- [76] J. Allison *et al.* (Geant4 Collaboration), Nucl. Instrum. 699 Methods Phys. Res., Sect. A **835**, 186 (2016).
- [77] See Supplemental Material at [please.insert.a.url](#) for 699 a data release for information shown in Figs. 2, 4, and 5.
- [78] D. S. Akerib *et al.* (LZ Collaboration), Phys. Rev. C **102**, 699 014602 (2020).
- [79] D. Akerib *et al.* (LZ Collaboration), Phys. Rev. D **101**, 699 052002 (2020).
- [80] D. Akerib *et al.* (LZ Collaboration), Phys. Rev. D **104**, 699 092009 (2021).
- [81] P. Faulkner *et al.*, J. Phys. G **32**, N1 (2005).
- [82] D. Britton *et al.*, Philos. Trans. R. Soc. A **367**, 2447 699 (2009).

Supplemental Materials

DETAILED EVENT RATES

TABLE S1. Number of events remaining after each stage of event selection criteria described in the main text.

Selection description	Events after selection
All triggers	1.1×10^8
Analysis time hold-offs	6.0×10^7
Single scatter	1.0×10^7
Region-of-interest	1.8×10^5
Analysis cuts for accidentals	3.1×10^4
Fiducial volume	416
OD and Skin vetoes	335

TUNED DETECTOR AND XENON RESPONSE MODEL DETAILS

The LZ detector and xenon response models are implemented in a NEST-based application that includes effects such as curved electron drift paths from field non-uniformities, finite position reconstruction resolution in the transverse (x, y) and longitudinal z directions, and position-dependence in S1 and S2 areas. The key numerical parameters of the NEST model are provided in Table S2. Additionally, a header file for NEST 2.3.7 that will reproduce the ER and NR response models used in this analysis is available online at [please.insert.a.url](#). Note that the extraction field number is known to be an effective value due to multiple models for this effect in NEST, and this parameter is tuned such that the extraction efficiency matches the LZ data.

In addition to the parameters below, the width of the predicted ER and NR bands had to be reduced to match LZ calibration data and, as mentioned in the main text, the NEST recombination skewness model was turned off. There are detailed instructions for implementing these changes in the provided header file.

TABLE S2. NEST tuning parameters. Parameters in the top half of the table are input parameters, while bottom half parameters result from NEST calculations.

Parameter	Value
g_1^{gas}	0.0921 phd/photon
g_1	0.1136 phd/photon
Effective gas extraction field	8.42 kV/cm
Single electron	58.5 phd
Extraction Efficiency	80.5 %
g_2	47.07 phd/electron

DATA RELEASE

Selected data from the following plots from this paper are available at [please.insert.a.url](#).

- Figure 2: points representing the total efficiency curve for this analysis (black line).
- Figure 4: points in S1-S2 space representing the data used in the WIMP search (black points).
- Figure 5: WIMP mass points with measured 90% confidence limits and median and 1 and 2 sigma sensitivity bands.